Distributed Aberration Correction Techniques Based on Tomographic Sound Speed Estimates

Rehman Ali, *Student Member, IEEE*, Thurston Brevett, *Student Member, IEEE*, Dongwoon Hyun, *Member, IEEE*, Leandra L. Brickson, *Student Member, IEEE*, and Jeremy J. Dahl, *Senior Member, IEEE*

***Abstract*— Phase aberration is widely considered a major source of image degradation in medical pulse-echo ultrasound. Traditionally, near-field phase aberration correction techniques are unable to account for distributed aberrations due to a spatially varying speed of sound in the medium, while most distributed aberration correction techniques require the use of point-like sources and are impractical for clinical applications where diffuse scattering is dominant. Here, we present two distributed aberration correction techniques that utilize sound speed estimates from a tomographic sound speed estimator that builds on our previous work with diffuse scattering in layered media. We first characterize the performance of our sound speed estimator and distributed aberration correction techniques in simulations where the scattering in the media is known *a priori*. Phantom and *in vivo* experiments further demonstrate the capabilities of the sound speed estimator and the aberration correction techniques. In phantom experiments, point target resolution improves from 0.58 to 0.26 and 0.27 mm, and lesion contrast improves from 17.7 to 23.5 and 25.9 dB, as a result of distributed aberration correction using the eikonal and wavefield correlation techniques, respectively.**

***Index Terms*— Distributed aberration, phase aberration correction, ray tracing, speed of sound.**

I. Introduction

PHASE aberration has been identified as one of the major sources of image degradation in medical ultrasound imaging and is ultimately caused by sound speed variations in human tissue, which are known to vary by up to 10% [1]. Several simplifying models have been proposed for phase aberration, two of which are the near-field and mid-field phase screen models. The near-field phase screen model assumes that all phase aberration is modeled by a thin film at the transducer surface. This effectively perturbs transmit and receive delays by the same amount everywhere in the ultrasound image. Many phase aberration correction techniques assume the near-field phase screen model when measuring and correcting for phase aberration [2]. These techniques measure a single set of aberration delays that affects each transducer element and apply compensating delays to each transducer element to correct the image.

The mid-field phase screen also assumes that phase aberration is primarily due to a thin film; however, this thin film is placed at some depth away from the transducer surface. As a result, the aberration delays are no longer fixed for each transducer element as a function of the imaging location. Time-shift compensation based on aberrations over a geometric path and backpropagation of the received wavefront using the angular spectrum method is one of the methods proposed to measure and correct distributed aberrations caused by a mid-field phase screen [3]. For this approach, the depth of the phase screen as well as its aberration delays has to be estimated before image correction can be applied. Neither phase-screen model, however, accurately captures the spatial distribution of sound speed heterogeneity in biological tissue. In addition, these early distributed aberration correction techniques were impracticable because they relied on coherent wavefronts for distributed correction and expensive hardware additions such as per-channel arbitrary waveform generators and could only correct at the point of measurement.

Aberration is generally due to a spatially varying sound speed distribution as opposed to a single thin film. Locally adaptive phase aberration correction techniques [4] treat distributed aberration as a spatially varying near-field phase screen. This approach, while aware of the spatially varying sound speed distribution of the medium as the source of aberration, makes no attempt to model aberration delays based on the sound speed distribution. Knowledge of the speed of sound in the medium may be used to achieve distributed aberration correction by enforcing an image formation model that remains physically consistent with an estimated speed of sound. For example, a delay-and-sum (DAS) beamformer may use a set of corrected delays based on the true speed of sound in the medium [5]. Alternatively, a diffraction-based approach [6], [7] can passively achieve distributed aberration correction by propagating signals according to the sound speed

Manuscript received November 22, 2021; accepted March 24, 2022. Date of publication March 30, 2022; date of current version April 26, 2022. This work was supported in part by the Stanford-Philips Research Collaboration, in part by the National Defense Science and Engineering Graduate (NDSEG) Fellowship, and in part by the National Institute of Biomedical Imaging and Bioengineering (NIBIB) under Grant R01-EB027100. *(Corresponding author: Rehman Ali.)*

This work involved human subjects or animals in its research. Approval of all ethical and experimental procedures and protocols was granted by the Institutional Review Board and the Stanford University's Institutional Administrative Panel on Laboratory Animal Care.

Rehman Ali, Thurston Brevett, and Leandra L. Brickson are with the Department of Electrical Engineering, Stanford University, Palo Alto, CA 94305 USA (e-mail: rali8@stanford.edu; tbrevett@stanford.edu; llbricks@stanford.edu).

Dongwoon Hyun and Jeremy J. Dahl are with the Department of Radiology, School of Medicine, Stanford University, Palo Alto, CA 94304 USA (e-mail: dongwoon.hyun@stanford.edu; jjdahl@stanford.edu).

Digital Object Identifier 10.1109/TUFFC.2022.3162836

in the medium. Since either approach to distributed aberration correction depends on accurate sound speed estimates, the choice of sound speed estimator plays a critical role.

One group of sound speed estimators uses aberration delays to estimate perturbations to the speed of sound in the medium [8]–[11]. While these approaches can detect and measure lateral variations in sound speed, accurate measurement of the speed of sound in axially varying media can be challenging [12]. Another group of techniques assumes negligible variation in the speed of sound laterally [5], [13]–[15] and can often accurately estimate the speed of sound in layered media with axial variations in the speed of sound but often performs poorly when substantial lateral variations are present. Recently, we have attempted to improve these estimators when lateral sound speed changes are present [16].

Recent approaches to distributed aberration correction have used sound speed estimates to drive phase aberration correction [5], [10], [17]. These aberration correction methods compute beamforming delays assuming that sound travels on straight line compute beamforming delays assuming that sound travels on straight line paths [10], [17] or using a set of refraction-corrected delays based on the eikonal equation [5], [16], [18]. These latter methods have shown improvements in resolution and contrast as a result of refraction correction in the delay computation.

In this article, we incorporate a tomographic sound speed estimator [16] to improve robustness to lateral sound speed variations in the sound speed estimator component of our distributed aberration correction techniques. We also introduce an additional distributed aberration correction technique that utilizes the estimated sound speed distribution that uses wave propagation to spatially align transmit and receive wavefronts. We extend the analysis of our refraction correction method [5], as well as the wave propagation method, to validate these distributed aberration correction techniques in simulations and phantom experiments with known speed of sound. We further apply these techniques in animals and humans to demonstrate their *in vivo* performance.

II. Theory

A. Tomographic Sound Speed Reconstruction

We assume that the variations in the sound speed are small relative to the average sound speed over the path of propagation, thereby allowing us to neglect the effects of refraction. Assuming that sound travels on a straight ray path from the ith transducer element at $(x_i, 0)$ to a focal point (x_f, z_f), the travel time τ_i can be calculated as

$$\tau_i(x_f, z_f) = \int_0^{D_i(x_f,z_f)} \frac{dr}{c\left(x_i + \frac{r(x_f - x_i)}{D_i(x_f,z_f)}, \frac{r z_f}{D_i(x_f,z_f)}\right)} \quad (1)$$

where $D_i(x_f, z_f) = ((x_f - x_i)^2 + z_f^2)^{1/2}$ is the path length, $c(x, z)$ is the speed of sound at (x, z), and dr is increment along the path from $(x_i, 0)$ to (x_f, z_f). The line integral in (1), indexed over all transducer elements and focal points, can be used to form a linear system of equations that relates individual pixels in the sound speed distribution of the medium to the travel time observed over each path

$$\vec{t}_{\text{obs}} = \boldsymbol{H}\vec{s} \quad (2)$$

where the slowness vector $\vec{s}$ is a vectorization of $[1/(c(x, z))]$, $\boldsymbol{H}$ is a matrix that encodes the line integrals between every transducer element and focal point, and $\vec{t}_{\text{obs}}$ is a vector of the travel times observed over those propagation paths [see (1)]. This linear system defines an ill-conditioned inverse problem whose goal is to recover $c(x, z)$ in the medium from the measured travel times. Because phase aberration is the mechanism by which the travel times are measured, we will refer to this tomographic framework for sound speed reconstruction as inverse-modeled phase aberration computed tomography (IMPACT).

As part of IMPACT, we reframe the solution of (2) as a Bayesian maximum likelihood estimation problem [19]. First, the residuals $\vec{t}_{\text{obs}} - \boldsymbol{H}\vec{s}$ are modeled as a normal random variable with mean $\vec{0}$ and covariance $\boldsymbol{R}$, which is a diagonal matrix whose entries are proportional to $D_i(x_f, z_f)$. The purpose of scaling the variance of the observations with propagation distance is to account for the decrease in SNR due to geometric spreading of the wave along the path of propagation. Second, we model the prior distribution over $\vec{s}$ as normal random variable with mean $\vec{s}_{\text{prior}} = (1/(1540\ (\text{m/s})))$ and covariance $\boldsymbol{Q}$. Rather than directly implementing $\boldsymbol{Q}$ as a full matrix, $\boldsymbol{Q}$ is implemented implicitly as a convolution with a Gaussian blurring kernel. The Gaussian blurring kernel encodes the covariance between neighboring pixels in the slowness image and maintains the smoothness of the reconstruction. Maximizing the posterior likelihood results in the following least-squares reconstruction problem:

$$\min_{\vec{s}} \left\{ \frac{1}{2}(\vec{t}_{\text{obs}} - \boldsymbol{H}\vec{s})^T \boldsymbol{R}^{-1} (\vec{t}_{\text{obs}} - \boldsymbol{H}\vec{s}) + \frac{1}{2}(\vec{s} - \vec{s}_{\text{prior}})^T \boldsymbol{Q}^{-1} (\vec{s} - \vec{s}_{\text{prior}}) \right\}. \quad (3)$$

The closed-form solution to this least-squares reconstruction problem is

$$\vec{s} = \vec{s}_{\text{prior}} + \boldsymbol{Q}\boldsymbol{H}^T(\boldsymbol{H}\boldsymbol{Q}\boldsymbol{H}^T + \boldsymbol{R})^{-1}(\vec{t}_{\text{obs}} - \boldsymbol{H}\vec{s}_{\text{prior}}) \quad (4)$$

which can be broken into two parts

$$(\boldsymbol{H}\boldsymbol{Q}\boldsymbol{H}^T + \boldsymbol{R})\xi = \vec{t}_{\text{obs}} - \boldsymbol{H}\vec{s}_{\text{prior}} \quad (5)$$

$$\vec{s} = \vec{s}_{\text{prior}} + \boldsymbol{Q}\boldsymbol{H}^T\xi \quad (6)$$

where ξ is an intermediate term determined by solving (5) using conjugate gradient. The resulting ξ is then used in (6) to update the prior slowness distribution. Note that in this form, $\vec{t}_{\text{obs}} - \boldsymbol{H}\vec{s}_{\text{prior}}$ contains the observed aberration delays. Although the tomographic inversion problem may be posed entirely in terms of slowness by relating the pixelwise slowness to the mean slowness over each path, the current formulation of IMPACT also models time shifts between receive elements as aberration delays.

B. Aberration Correction Based on Eikonal Equation Travel Times

Given the sound speed $c(x, z)$ in the medium, the travel time between a point (x, z) in the medium and a transducer element at $(x_i, 0)$ can be found using the eikonal equation

$$\sqrt{\left(\frac{\partial \tau}{\partial x}\right)^2 + \left(\frac{\partial \tau}{\partial z}\right)^2} = \frac{1}{c(x,z)} \tag{7}$$

subject to the boundary condition $\tau(x_i, 0) = 0$. This is repeated for each element i on the array so that all beamforming delays $\tau_i(x, z)$ are known for every point (x, z) in space. By accounting for sound speed heterogeneity in the medium, these beamforming delays should correct for phase aberration. The eikonal equation (7) accurately models refraction and can be solved efficiently using the fast marching method [18].

C. Aberration Correction by Wavefield Correlation

The angular spectrum method [20] is a technique for simulating the wavefield based on signals transmitted or received by a transducer array. The wavefield can be used for imaging by correlating the transmit and receive wavefields as described in [21]. Here, we extend the angular spectrum method to laterally heterogeneous media by using the Fourier split-step method [7], [20]–[23]. The transmitted and received wavefields are described by the following equations:

$$\begin{aligned} p_{tx(i)}(x, z+\Delta z, f) = {} & W(x) S_-(x, z, f) \mathcal{F}^{-1}_{k_x \mapsto x} \\ & \times H_-(k_x, z, f) \mathcal{F}_{x \mapsto k_x} p_{tx(i)}(x, z, f) \end{aligned} \tag{8}$$

$$\begin{aligned} p_{rx(i)}(x, z+\Delta z, f) = {} & W(x) S_+(x, z, f) \mathcal{F}^{-1}_{k_x \mapsto x} \\ & \times H_+(k_x, z, f) \mathcal{F}_{x \mapsto k_x} p_{rx(i)}(x, z, f) \end{aligned} \tag{9}$$

$$H_\pm(k_x, z, f) = \exp\left(\pm j 2\pi \left(\frac{f^2}{\bar{c}^2(z)} - k_x^2\right)^{1/2} \Delta z\right) \tag{10}$$

$$S_\pm(x, z, f) = \exp\left(\pm \frac{j 2\pi f \Delta z}{c_{\text{res}}(x, z)}\right) \tag{11}$$

$$\frac{1}{\bar{c}(z)} = \int_{-L/2}^{L/2} \frac{dx}{c(x,z)} \tag{12}$$

$$\frac{1}{c_{\text{res}}(x,z)} = \frac{1}{c(x,z)} - \frac{1}{\bar{c}(z)} \tag{13}$$

where $W(x)$ is a window function used to suppress the wraparound caused by the discrete Fourier transform.

Propagation via the angular spectrum method should correct for aberration by accounting for the true speed of sound in the medium. Ray-based methods such as the eikonal correction cannot account for the temporal splitting of the wavefront as a result of focusing effects or sound speed heterogeneities in the medium. By accounting for the full waveform, the wavefield correlation method can correct for both phase and amplitude distortions in the wavefronts such as wavefront splitting as a result of a spatially varying speed of sound.

III. Methods

A. Sound Speed Estimation and Phase Aberration Correction

Multistatic synthetic aperture channel data were synthetically transmit focused at all points in the ultrasound image at sound speeds ranging from 1400 to 1700 m/s in 1 m/s steps. The focused, or delayed, channel data were summed across transmit channels to form complex receive channel data for each imaging point. Coherence factor (CF) [24], which is given as

$$\text{CF} = \frac{\left|\sum_{k=1}^{N} s[k]\right|^2}{N \sum_{k=1}^{N} |s[k]|^2} \tag{14}$$

where $s[k]$ are complex samples from each of N receive channels, was computed for each imaging point and sound speed. The CF images at each sound speed are spatially smoothed using a Gaussian blurring kernel (full-width at half-maximum (FWHM) = 3.8 and 2.0 mm in the x- and z-directions, respectively) in order to mitigate measurement noise. The focusing sound speed (which we refer to as an effective "average sound speed") that maximizes CF at each focal point was used to obtain $\vec{t}_{\text{obs}}$ by scaling the distances between the transducer elements and focal points by this focusing speed of sound. However, if the maximum CF was below 0.1, the corresponding focal point was removed from the tomographic reconstruction process. This threshold on the CF was used to avoid anechoic regions in the reconstruction process that do not contain reflections that can be used to compute average sound speed estimates. $\vec{t}_{\text{obs}}$, calculated from the average sound speed estimates, was then used to obtain the local speed of sound by solving (5) and (6). The Gaussian blurring kernel used for $\boldsymbol{Q}$ had an FWHM = 9.9 and 3.9 mm in the x- and z-directions, respectively. The resulting local sound speed estimates are used to perform phase aberration correction using either eikonal correction or wavefield correlation.

TABLE I
k-Wave Simulation Settings

Parameter	Value	Units
Array Geometry	Linear	-
Number of Elements	128	elements
Element Pitch	0.15	mm
Element Kerf	0	mm
Center Frequency	4 or 8	MHz
Fractional Bandwidth	0.7	-
Sampling Frequency	85.56	MHz
Grid Spacing	0.03	mm

B. k-Wave Simulations in Heterogeneous Media

The multistatic synthetic aperture dataset was simulated in k-Wave [25] for diffuse scattering in several heterogeneous media both to examine the accuracy of the IMPACT sound speed estimator and the capabilities of each aberration correction technique. The Hilbert transform was applied to the multistatic dataset to obtain an analytic representation of the channel signals. Simulation parameters, such as the transducer configuration, transmit pulse, computational grid, and sampling, are described in Table I.

Simulations were used to demonstrate the performance of the IMPACT sound speed estimator in diffuse scattering media with layered speed of sound. These simulations consisted of four-layer media (A and B), an eight-layer medium (C), and layered media (D and E) with mild lateral sound speed variations.

Another series of simulations was used to examine the efficacy of distributed aberration correction based on an estimated speed of sound. These simulations consisted of a heterogeneous sound speed map using an abdominal wall model in [26]. Here, we blur the sound speed map using a Gaussian kernel with the FWHM of 0, 3, 6, 9, 12, and 24 mm to vary the degree of lateral sound speed variation in the medium. A 5 $\times$ 5 grid of point targets (spaced 3.5 mm axially and 4.0 mm laterally) were used in the simulations to quantify the performance of distributed aberration correction as the degree of lateral sound speed variation (and the resulting performance of IMPACT) in the medium is varied.

C. Metrics and Evaluation

To quantify image quality, we utilized the shift in the point targets from their true location, measured as the radial difference in the location of peak intensity from the true location of the point target, and the −6-dB lateral beamwidth (FWHM resolution) of each point target. Quantitative results were compared using the eikonal beamformer with the known sound speed (best possible correction), a constant sound speed (conventional beamforming), and the estimated sound speed (aberration corrected).

In order to isolate the point targets from background speckle for accurate measurements, we repeated each simulation without diffuse scattering and, where necessary, applied the IMPACT sound speed estimates from the diffuse scatterer simulations. An iterative method was used to detect the location of peak magnitude for each point target as well as the 6 dB width of each target. In cases where the beam is severely degraded (the peak magnitude was less than 13 dB of the original magnitude), the image of the point target no longer resembles a sinc function and the algorithm fails to detect the location or 6-dB beamwidth. These points were marked as undetected and excluded from the calculations.

D. Experimental Data Acquisition

Two transmit sequences were implemented on the Verasonics Vantage 256 scanner using the L12-3v probe. The first sequence was a multistatic synthetic aperture transmit sequence, consisting of receive channel data for each single-element transmit. The second sequence was a walking-aperture focused-transmit sequence with multiple focal depths, as described in Table II. The multistatic synthetic aperture dataset was recovered from this multifocal walking-aperture transmit sequence using the regularized inversion technique described in [27].

In phantom experiments, a slab of pork was placed on top of an ATS Model 549 phantom (1460 m/s) to test the IMPACT sound speed estimator and distributed aberration correction techniques in the presence of sound speed heterogeneity with both transmit sequences. *In vivo* datasets were also acquired from the abdomen of obese Zucker rats and the thyroid gland in a healthy human volunteer. In the rat imaging case, the multifocal walking-aperture transmit sequence was used, and a multistatic synthetic aperture dataset was recovered. In the human thyroid imaging case, a multistatic synthetic aperture sequence was used to acquire channel data using only the center 128 elements of the L12-3v probe.

TABLE II
MULTIFOCAL WALKING-APERTURE TRANSMIT SEQUENCE ON VERASONICS L12-3V

Parameter	Value	Units
Array Geometry	Linear	-
Number of Elements	192	elements
Element Pitch	0.2	mm
Center Frequency	7.8	MHz
Focal Depths	17.8, 29.6, 41.5	mm
Transmit Angle	0	Degrees
Beam Origin Range	[-19.1, 19.1]	mm
Beam Origin Step	1	element
Aperture Width (Around Beam Origin)	128	elements
Transmit Apodization	Rectangular	-

IV. RESULTS

A. Sound Speed Estimation Using IMPACT

Fig. 1 shows the performance of the IMPACT sound speed estimator in five media: A, B, C, D, and E. Media A, B, and C are four-, five- and eight-layer media. The first row of Fig. 1 shows the ground-truth simulated speed of sound. The second row of Fig. 1 shows the IMPACT reconstructed speed of sound when the exact average speed of sound is known at each focal point. These results are intended to understand the ideal performance of IMPACT when the exact average speed of sound is known for each focal location. The root-mean-square (rms) errors in the IMPACT reconstruction under these ideal conditions are 4.1 m/s (media A), 3.7 m/s (media B), 5.2 m/s (media C), 3.5 m/s (media D), and 4.9 m/s (media E). The third row of Fig. 1 shows the IMPACT reconstructed speed of sound when the CF maximization process is used to obtain the average speed of sound. The rms error in sound speed estimation is 6.3, 8.6, and 7.9 m/s for media A, B, and C, respectively. The increase in the number of layers from media A to C serves to demonstrate the axial resolution of the IMPACT sound speed estimator in terms of the thickness of each layer. Media D and E incorporate lateral variations in the speed of sound and have the highest rms errors (12.8 and 17.1 m/s, respectively). In addition, the rms error in the speed of sound is larger from 20 to 35 mm depth than from 5 to 20 mm depth in media D and E. In each medium, IMPACT is the most inaccurate at the deepest depths where the fewest time-of-flight measurements contribute to the sound speed estimate. The selection of $\vec{s}_{\text{prior}}$ was shown to have no effect on sound speed estimation (data not shown).

B. Aberration Correction Based on Estimated Sound Speed

Fig. 2 shows the effect of applying IMPACT sound speed estimations for aberration correction to the series of abdominal wall simulations with decreasing lateral variations in the true speed of sound. As the lateral variation in the ground-truth

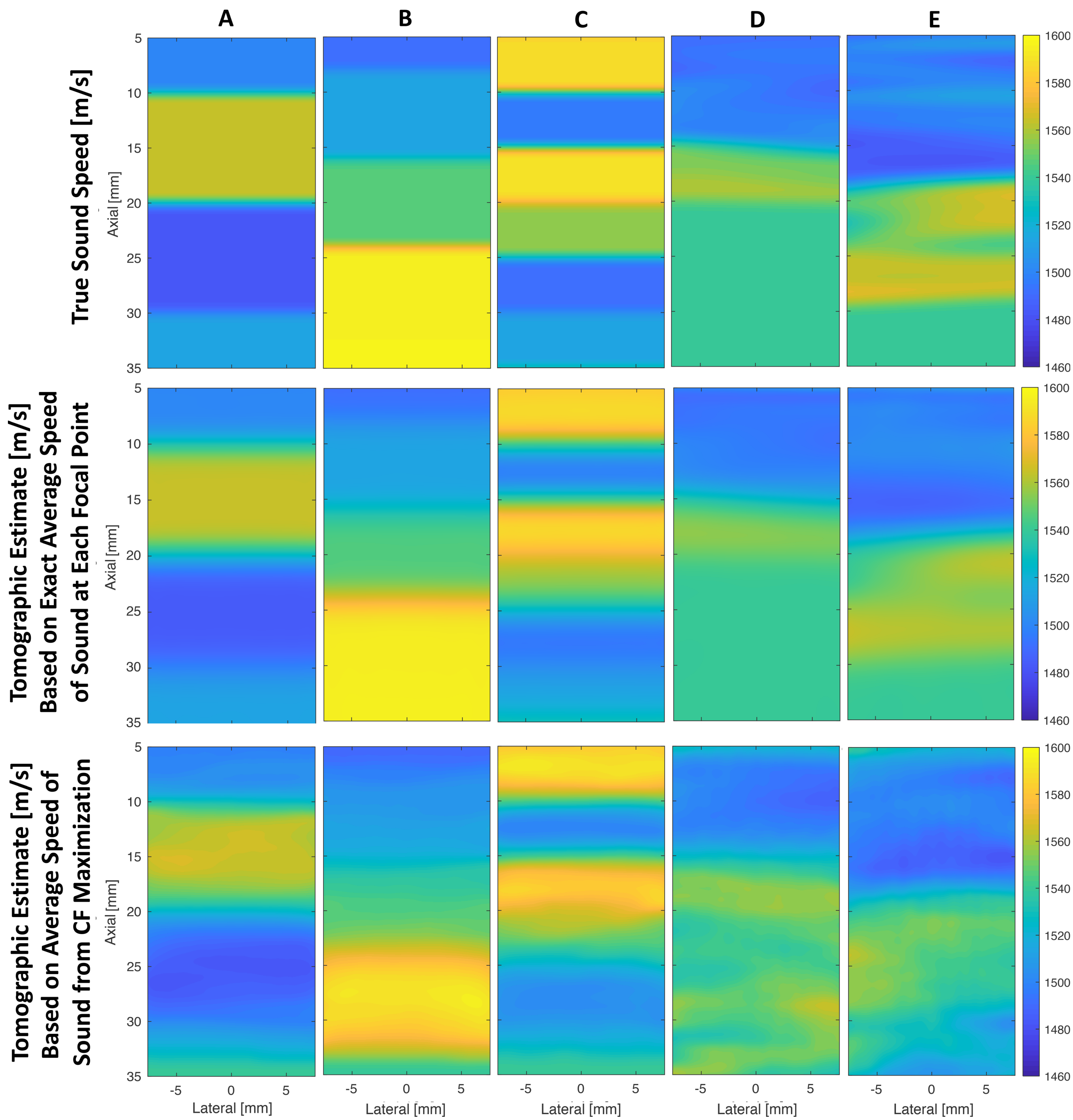

Fig. 1. Sound speed estimation in heterogeneous media Using IMPACT. Diffuse scattering was simulated in five media labeled A, B, C, D, and E. The top row show the true sound speed in the medium. The middle row shows the IMPACT sound speed estimates when the exact average speed of sound is known for each focal point. The bottom row shows the IMPACT sound speed estimates from the average speed of sound obtained by CF maximization. When IMPACT is applied to the exact average speed of sound at each focal point, the rms error in sound speed estimation is 4.1 m/s (A), 3.7 m/s (B), 5.2 m/s (C), 3.5 m/s (D), and 4.9 m/s (E). When IMPACT is applied to the average speed of sound from CF maximization, the rms error in sound speed estimation is 6.3 m/s (A), 8.6 m/s (B), 7.9 m/s (C), 12.8 m/s (D), and 17.1 m/s (E). In media D and E, the rms error in the IMPACT estimate using the CF maximization process is 8.2 m/s (D) and 9.8 m/s (E) from 5 to 20 mm depth and 17.4 m/s (D) and 24.3 m/s (E) from 20 to 35 mm depth.

speed of sound decreases, the IMPACT estimates become more accurate. Visually, it is observed that the structure of the sound speed also approaches the structure of the true sound speed as the medium exhibits less lateral variation in the sound speed. For deeper point targets where the sound speed estimate is highly inaccurate, point targets exhibit a much lower intensity as the signal becomes highly incoherent. In the FWHM $=0$ mm case, the leftmost point target at 31.5 mm depth and the three leftmost point targets at 36 mm depth could not accurately be localized in the image when aberration correction was applied using the IMPACT sound speed estimate. In the FWHM $=3$ mm case, only the leftmost

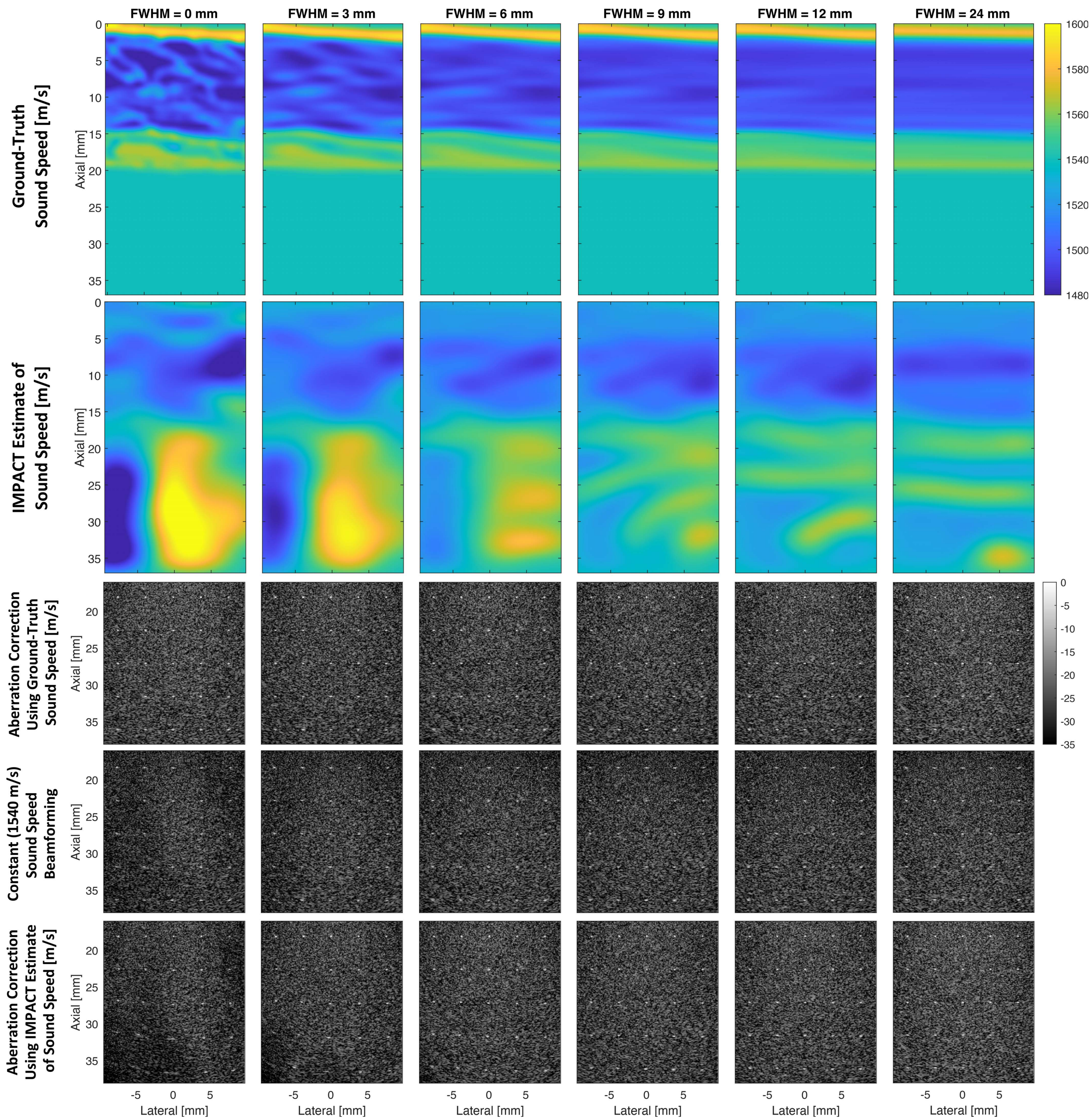

Fig. 2. Effect of sound speed estimation error on distributed aberration correction. The IMPACT method applied to a simulated abdominal wall model with increasing lateral blurring from left to right. The eikonal equation was used to beamform B-mode images using the true sound speed, a constant 1540-m/s sound speed, and the estimates from IMPACT. The FWHM corresponds to the Gaussian kernel used to laterally blur the sound speed. A large FWHM causes sound speed to more closely resemble a layered medium.

target at 36 mm depth could not be localized in the image after aberration correction using the IMPACT estimate was applied. These point targets were omitted from the following analyses.

Fig. 3 shows the localization error of the point targets, relative to the true position of the point targets, for eikonal beamforming with different sound speed maps with decreasing lateral blurring of the ground-truth speed of sound. Using the ground-truth sound speed profile, the localization error is small and increases at a rate of approximately 1 μm per millimeter depth and about 0.64 μm per millimeter of lateral blurring kernel. For a constant sound speed, the localization error is greater than 300 μm for all depths. Lateral variations in the speed of sound appeared to have a small, and potentially negligible, effect on localization error. The estimated sound speed from IMPACT shows a localization error less than 100 μm for media that more closely approximate layered media but increases drastically with depth for media with more lateral variation.

Fig. 4 shows the percent increase in point target width relative to the ideal case where ground-truth speed of sound is

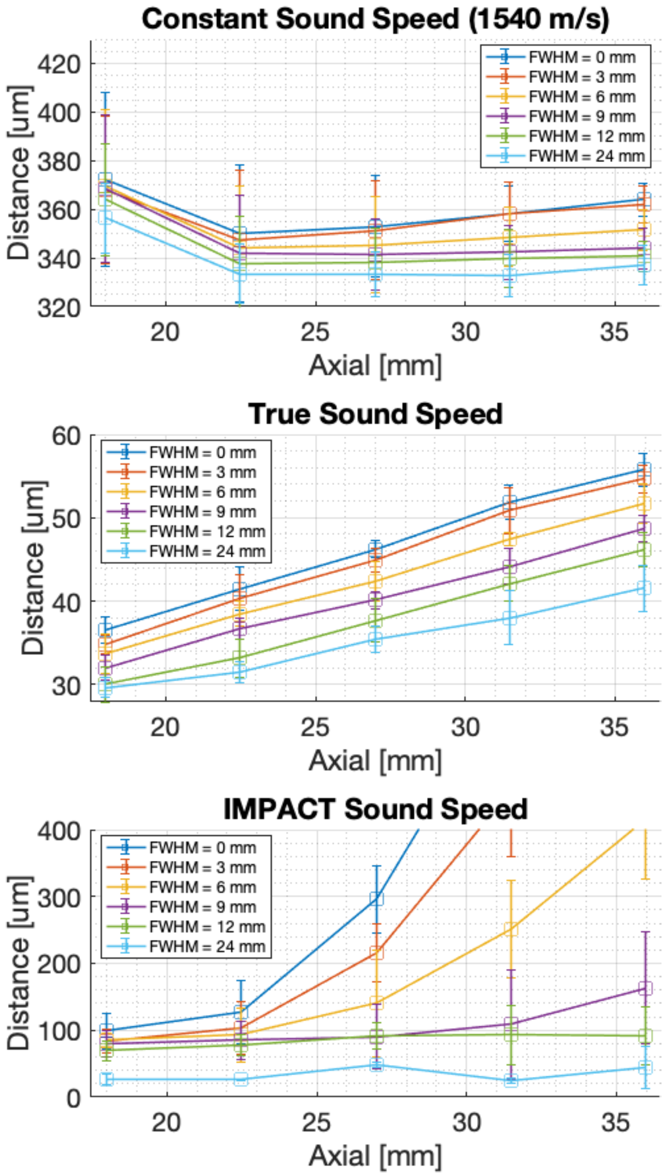

Fig. 3. Point target location error from distributed aberration correction in Fig. 2. The mean and standard deviation of the error between the true location of the point target and the location of the point's peak magnitude in the image for eikonal beamforming with each set of sound speed maps. The mean and standard deviation are taken over the five lateral points for each depth.

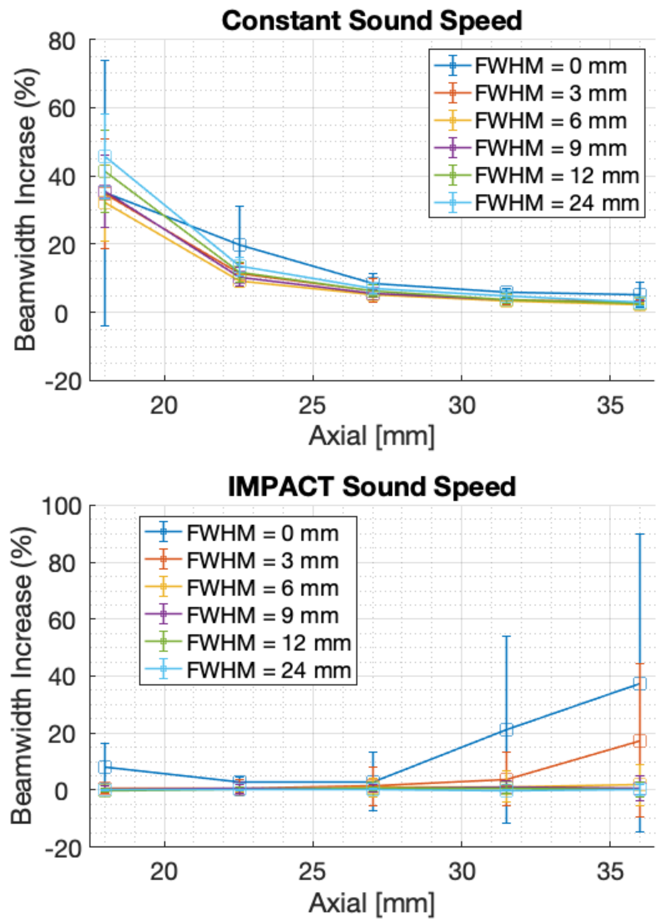

Fig. 4. Point target resolution from distributed aberration correction in Fig. 2. The mean and standard deviation, over the lateral five point targets at each depth, of the percent increase in the −6-dB beamwidth relative to the ideal point target (with known speed of sound).

known. For eikonal beamforming with a constant sound speed (1540 m/s), there is a large increase in point target width at the shallowest depth for this medium and the difference improves with depth into the medium. The point target width resulting from aberration correction with the IMPACT sound speed estimate is the most accurate at the shallowest depth in the medium. When using the estimated sound speed from IMPACT, the increase in point target width remains close to 0% for media that more closely approximate layered media but increases with depth for media with more lateral variation.

Fig. 5 shows the complete aberration correction pipeline in a phantom where channel data, initially acquired from focused transmit beams, are optimally focused everywhere in the image by using multistatic synthetic aperture data (via REFoCUS) and IMPACT to estimate the speed of sound in the medium. IMPACT was used to estimate the speed of sound from the multistatic dataset recovered by REFoCUS. The sound speed estimated in the pork is around 1580 m/s, while the sound speed estimated within the phantom is roughly 1460 m/s. The image formed by coherently compounding focused transmits beams prior to multistatic dataset recovery is shown in Fig. 5(b), and images produced after multistatic dataset recovery are shown in Fig. 5(c). When the resulting multistatic dataset is focused at 1540 m/s, focusing only improves around 15 mm depth. However, when the estimated sound speed of the medium is used to focus the image, using either eikonal correction or wavefield correlation, the image is improved over all locations. The FWHM point target resolution at 35 mm depth improves by 0.3 mm after multistatic dataset recovery and further improves by about 0.3 mm for each aberration correction technique.

Fig. 6 shows sound speed estimation and aberration correction with multistatic channel data from a phantom with anechoic lesions. In addition to the sound speed change between the 5-mm slab of pork and the ATS phantom, the IMPACT estimator also detects sound speeds differences between the anechoic region and the speckle background. When this sound speed estimate is used for distributed phase aberration correction, the lesion boundaries and the bubbles trapped within

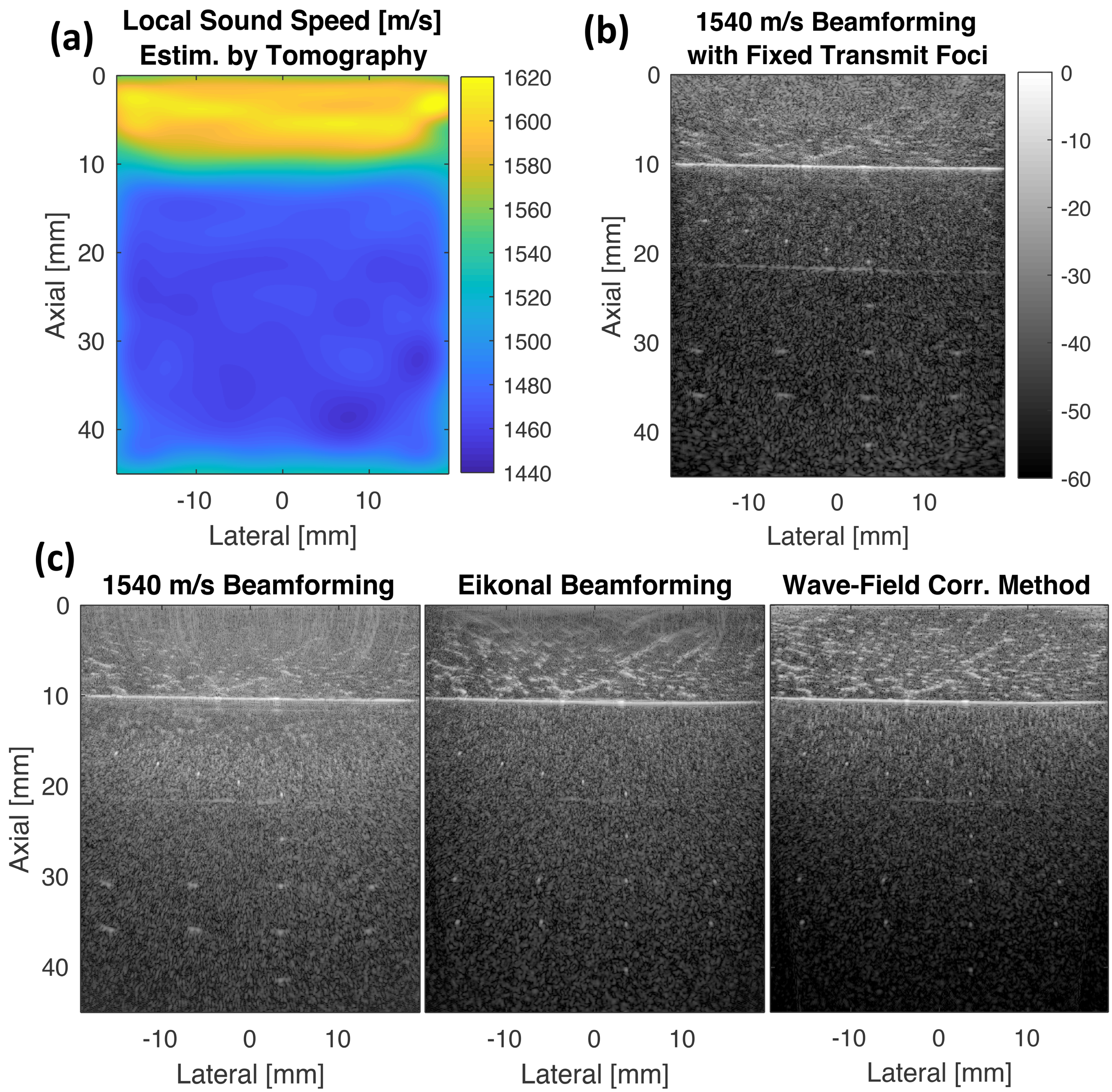

Fig. 5. Multistatic dataset recovery and distributed aberration correction with point targets. (a) IMPACT sound speed estimate based on the recovered multistatic dataset. (b) Coherent compounding of focused transmit beams (with 1540-m/s beamforming) prior to multistatic dataset recovery. (c) Demonstration of distributed aberration correction techniques after multistatic dataset recovery. FWHM point target resolution at 35 mm depth is (b) 0.88 mm and (c) 0.58, 0.26, and 0.27 mm from left to right for each of the three images.

the larger lesion are sharper and more clearly visible. Lesion contrast improves from 17.7 to 23.5 and 25.9 dB as a result of eikonal correction and wavefield correlation, respectively. However, the sound speed variations in the vicinity of the lesion likely have a negligible impact on the focusing of this region of the image. Because the results of aberration correction with both methods are similar, we omit the images from one of the methods in further figures for brevity.

Fig. 8 shows an *in vivo* example of sound speed estimation and phase aberration correction. There are three different views of the thyroid and carotid in a healthy human volunteer. Each image highlights thyroid nodules that change as a result of the aberration correction technique. The visibility of certain thyroid nodules appears to improve as a result of aberration correction. The shape and size of each thyroid nodule appear to change.

V. Discussion

We demonstrated two distributed phase aberration correction techniques that improve focusing in the image reconstruction based on the local speed of sound in the medium. However, the focusing improvement depends on the accuracy of the local sound speed used in aberration correction.

Because aberration correction depends on the accuracy of the sound speed estimator, we examine the strengths and weaknesses of the IMPACT sound speed estimator.

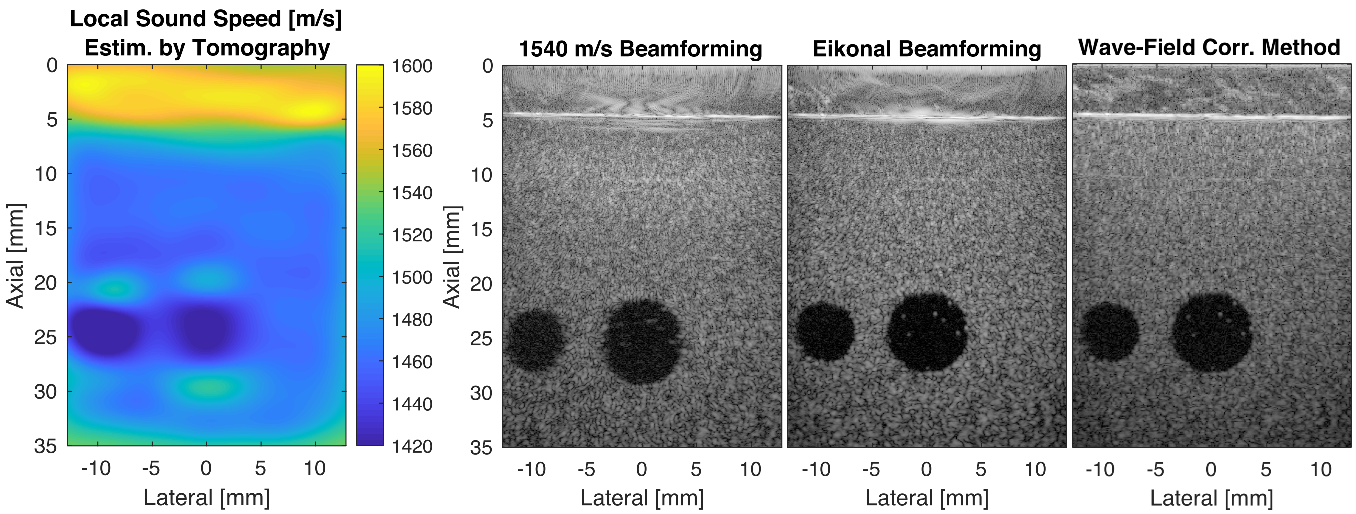

Fig. 6. Distributed phase aberration correction with anechoic lesions. The IMPACT estimator shows sound speed differences between the pork, the scattering material, and the anechoic lesions. Lesion contrast for the smaller lesion is 17.7 dB before aberration correction, 23.5 dB after aberration correction using travel times computed from the eikonal equation, and 25.9 dB after aberration correction using the wavefield correlation method.

When lateral sound speed variations are present in the medium, the superficial layers in the medium may add extra curvature to the travel times in $\vec{t}_{\text{obs}}$ observed at deeper depths. By separating the times of flight in $\vec{t}_{\text{obs}}$ along individual paths of propagation, IMPACT was designed so that point-wise variations in the average sound speed estimate would enable tomographic estimates of the speed of sound that could partially estimate lateral variations in the medium. However, because CF maximization relies on flattening the curvature of the coherent signal across the aperture to estimate the effective average speed of sound, the extra curvature caused by lateral variations in the superficial layers can bias the effective average sound speed estimate, which affects the reconstruction produced by IMPACT. As a result, the IMPACT sound speed estimate can drift away from the true value at greater depths in the medium due to lateral variations at shallow depths. In particular, characterizing the average speed-of-sound in a situation where the focus is split by lateral variations into multiple lobes would be a worst case scenario for the IMPACT method.

Seismic imaging approaches to wave velocity estimation can help identify approaches that can overcome the shortcoming of current sound speed estimation techniques used in ultrasound imaging. For example, layer-stripping methods [28], [29] estimate the wave velocity layer-by-layer in a way that remains consistent with estimates at shallower depths. However, these approaches can often be time consuming and often need special treatment to remain robust. Accurate and robust wave velocity estimation still remains an active area of research in both seismic and ultrasound imaging due to the difficulty of the inverse problem. In both seismic and ultrasound imaging, assumptions regarding the media are often used in order to simplify this inverse problem, and new techniques are often proposed to help overcome some of the limitations of these simplifying assumptions. Future work should build upon, or merge, existing techniques to improve sound speed estimation in as many cases as possible.

Despite these limitations, the IMPACT sound speed estimator was shown to sufficiently estimate the speed of sound in the medium for phase aberration in layered media (see Figs. 5 and 6). In simulation results (Figs. 2–4), point targets with a depth of less than 27 mm consistently exhibited superior localization error and point target resolution than with assuming a constant sound speed. For simulations with less lateral variation, the localization error was consistently roughly 3–6 times more accurate than assuming a constant sound speed, and point target resolution consistently agreed with the results from knowing the exact true sound speed in the medium. As the lateral variation increased however, the 6 dB width and localization error of point targets at further depths drastically increased as the cumulative sound speed error led to more defocusing of the beam. Despite lack of the ground-truth speed of sound for the *in vivo* images, Figs. 7 and 8 also show image improvements using the proposed phase aberration correction methodology. Fig. 5 shows that the IMPACT sound speed estimates can be used to optimally focus at all depths in the medium, whereas a particular global sound speed may only achieve good focusing at a fixed depth in the image. Fig. 6 shows that IMPACT induces artifacts in the speed of sound around the anechoic lesions, but these lateral variations in the sound speed estimate do not negatively affect the performance of IMPACT because they occur at greater depths in the medium, reducing their effect on the aberration correction techniques.

One limitation of the simulation study is that the analysis is based on a single speed of sound distribution. While this distribution is realistic for abdominal layers, like many aberration correction techniques, the results will depend on the target location and its resulting speed of sound distribution. Thus, deeper analysis would be required for the specific target application of the aberration correction technique.

As previously noted in [16] and [30], there is a dual relationship between sound speed reconstruction and the focusing quality. If a perturbation in sound speed leads to large changes in focusing quality, sound speed should be easy to estimate accurately; conversely, if a perturbation in sound speed has a negligible effect on focusing quality, sound speed becomes

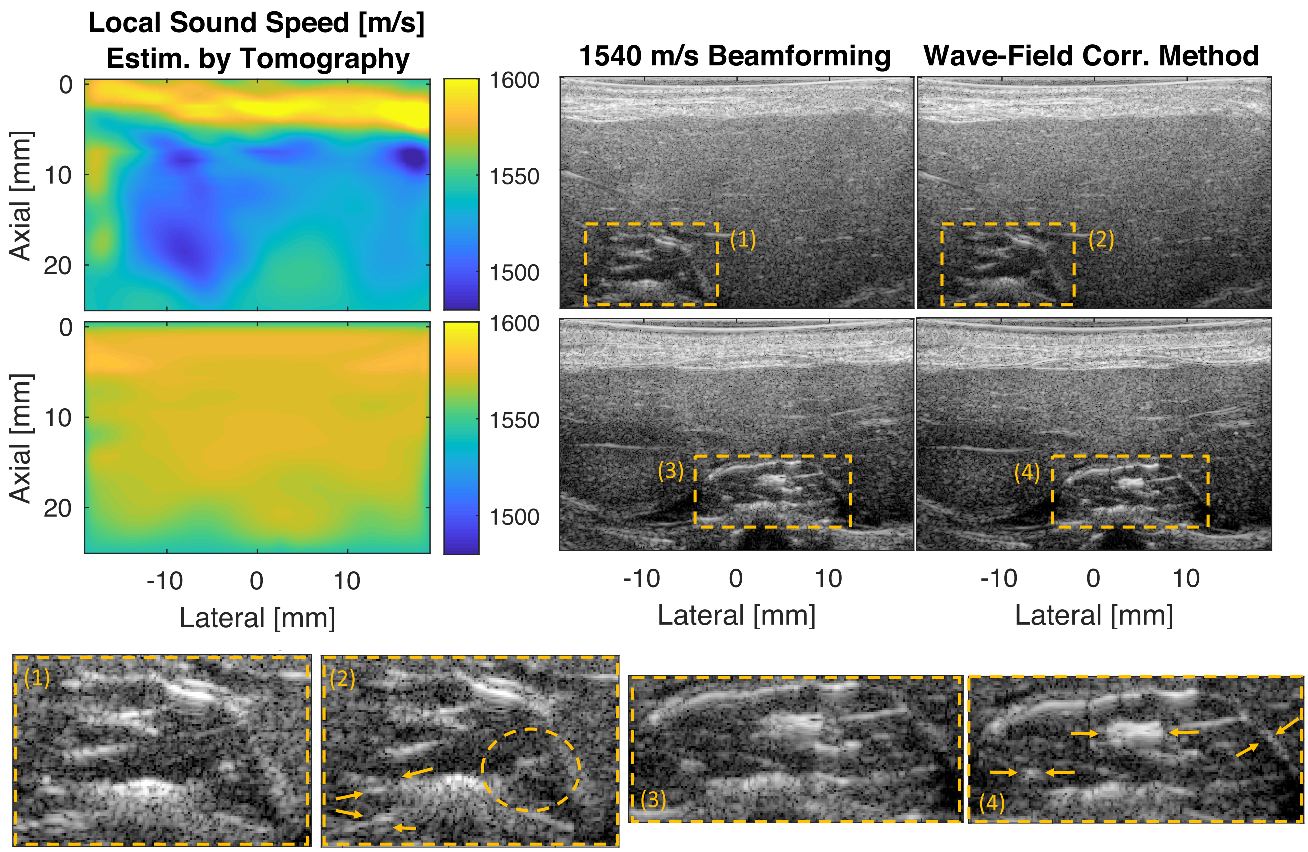

Fig. 7. Distributed phase aberration correction in the abdomen and vertebrae of obese Zucker rats. The global *ex vivo* sound speed measurement in the livers of each rat are 1527 m/s (top) and 1567 m/s (bottom). Aberration correction is performed using the wavefield correlation method. Similar changes are observed when using the eikonal equation to perform aberration correction. Boxes show zoomed-in views of the vertebrae in each image. Arrows and circles indicate locations where the resolution improves or new structures appear after aberration correction.

difficult to estimate accurately. When applying these principles to the tomographic estimation technique, it becomes clear that focusing quality in the image is largely insensitive to sound speed variations at the deepest depths in the medium; as a result, the tomographic reconstruction has large fluctuations at the deepest imaging depths.

Most of the phantoms shown in this study exhibit regions of uniform speckle. However, *in vivo* imaging examples often exhibit more complex structures. In particular, off-axis scattering from strongly reflecting structure may cause a slanting of arrival times if cross correlation methods were used to estimate phase aberration. The maximization of CF for estimating the average speed of sound helps to constrain the possible times of arrival at a particular point in the image to avoid this slanting of arrival times due to strongly reflecting structures. Although curved reflectors may be misconstrued as improperly focused point reflectors in the image, the multistatic synthetic aperture acquires multiple reflections from these curved reflectors so that the CF maximization method remains robust to the shape of the reflector.

One key difference between locally adaptive phase aberration correction techniques [4], [31] and distributed aberration correction techniques that use the IMPACT estimator is that the sound speed estimate physically constrains the observed phase aberration to be consistent with a single estimate of the sound speed in the medium. As a result, unlike previous approaches that used locally adaptive methods to perform aberration correction, the techniques employed in this article can correct the position and shape of imaging targets. Possible examples are seen in the top and bottom rows of Fig. 8. The shape of the thyroid nodules appears to change shape and position as a result of the sound speed correction. The sound speed estimate not only affects how the ultrasound signals are focused, but it also affects the shape of the structures being imaged because the aberration correction paradigm presented in this work directly affects the time of flight rather simply applying relative time delays to signals that were already focused using a potentially incorrect sound speed.

The distributed aberration correction techniques presented in this work are limited by the accuracy of the sound speed estimate, but the accuracy of the sound speed estimates are also limited by the achievable improvement in focusing quality throughout the image. This implies that the efficacy of the distributed aberration correction techniques is also affected by factors, such as frequency and f-number.

The main difference between the eikonal correction and the wavefield correlation method is the way that aberration correction is achieved. In the eikonal correction method, the delays applied to the signals in a DAS beamformer are calculated based on the eikonal equation for the estimated sound speed in the medium. However, for the wavefield correlation method, aberration correction is achieved by propagating and correlating transmit and receive signals in a numerically simulated medium with the estimated sound speed. As opposed to the

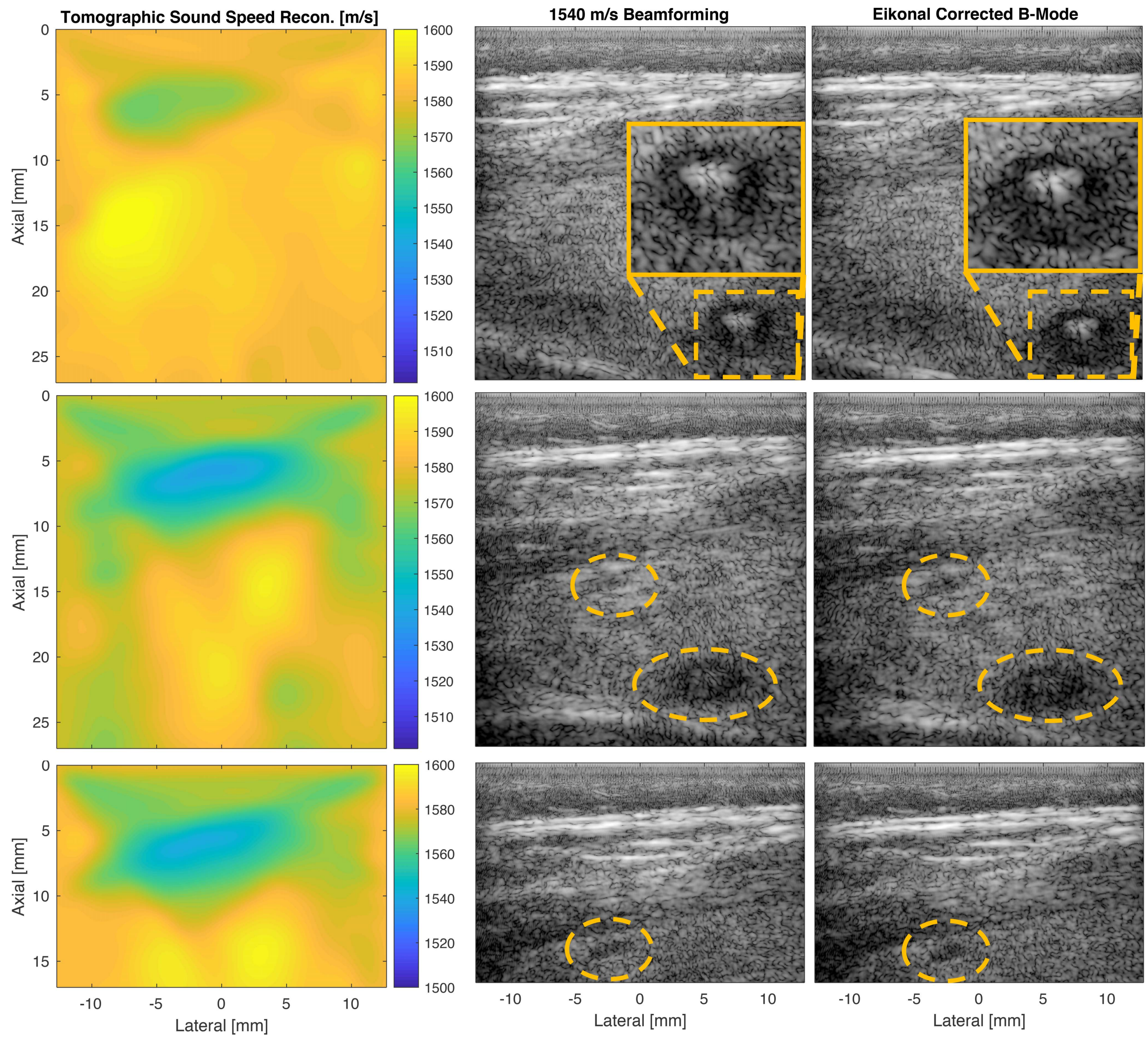

Fig. 8. Distributed phase aberration correction in human thyroid. Each row corresponds to a different imaging view of the thyroid. The boxes in the top row of B-mode images show zoomed-in views of a thyroid nodule with an inspissated colloid before and after phase aberration correction. The circles in the bottom two rows of images show visible changes in thyroid nodules as a result of phase aberration correction. Although phase aberration correction in these images was performed using the eikonal equation, each aberration correction method produced practically identical images.

eikonal correction method, the wavefield correlation method is not based on DAS beamforming, but rather a diffraction-based image reconstruction process. For this reason, the wavefield correlation method is far more computationally expensive [21] than the eikonal correction approach, which relies on DAS beamforming.

By accounting for the full waveform, the wavefield correlation method can correct for both phase and amplitude distortions in the wavefronts as a result of a spatially varying speed of sound. Ray-based methods such as the eikonal correction cannot account for the temporal splitting of the wavefront as a result of focusing effects or sound speed heterogeneities in the medium. In addition, the wavefield correlation method appears to remove near-field clutter in Figs. 5 and 6 because the correlation of transmit and receive wavefields gives less weight to receive events incident at large angles. While increasing the f-number used under the eikonal correction method could reduce near-field clutter, this will come at the cost of lower resolution at shallower imaging depths. In the wavefield correlation method, an f-number limit may be used to filter out transmit and receive events based on the angular spectrum of the signals [32]; however, we find that in these examples, the wavefield correlation process is enough to remove clutter without an explicit f-number limit. Furthermore, the Fourier-domain implementation of the wavefield correlation method is capable of fully deleting noise in frequency regions that refer to evanescent waves. Another aspect of the wavefield correlation method is that wave propagation is directly parameterized by the speed of sound in the medium. This may lead to a waveform-inversion-based approach for simultaneous sound speed estimation and phase aberration correction where the image formation process is differentiated with respect to the speed of sound in the medium to derive an update to the speed of sound in the medium and also improve focusing in the reconstructed image. For this reason, the wavefield correlation technique would be strongly preferred over the eikonal beamformation process in future work. A similar approach known as migration velocity analysis [33], [34] has been used in seismic imaging to reconstruct images of wave velocity and improve the focusing of reflectors.

One confounding factor in the experiments shown in Fig. 8 is the impact of reverberation clutter on both sound speed estimation and the aberration-corrected image. Despite diffuse reverberation clutter, the aberration correction techniques successfully improve the visibility of the smaller nodule at the top of the thyroid in the middle row of images. However, diffuse (or incoherent) reverberation clutter hinders and often overshadows the improvements resulting from phase aberration correction. Model-based [35], [36] and deep learning [37] solutions for clutter removal often do not account for phase aberration or sound speed variations in the medium. Future approaches to reverberation clutter removal should aim to preserve the underlying phase aberration while removing signals due to reverberation events. Preserving the underlying phase aberration would enable improved accuracy in sound speed estimation and aberration correction. *In vivo* ultrasound imaging is ultimately a multifaceted problem that requires a complete solution for viability in a clinical system.

VI. Conclusion

Sound speed estimates in a heterogeneous medium can be used to optimally focus an ultrasound image. Simulations show that if the exact sound speed distribution is known, aberration correction can be achieved in all parts of the ultrasound image. Both phantom and *in vivo* experiments show noticeable improvements in image quality when the estimated speed of sound is used to drive phase aberration correction. When sound speed was estimated in a layered medium, aberration was shown to be corrected in all parts of the ultrasound image based on those estimates using a ray-based and a diffraction-based correction scheme. In order to make our efforts more accessible to the broader research community, we have provided sample code and multistatic channel data for the point target phantom in Fig. 5 at github.com/rehmanali1994/DistributedAberrationCorrection (DOI: 10.5281/zenodo.4891861).

Acknowledgment

The authors would like to thank Joseph Jennings and Dr. Biondo Biondi from the Department of Geophysics and Dr. Peter Kitanidis from the Department of Civil and Environmental Engineering, Stanford University, Palo Alto, CA, USA, for their valuable scientific discourse.

References

[1] R. S. Cobbold, *Foundations of Biomedical Ultrasound*. London, U.K.: Oxford Univ. Press, 2006.

[2] S. W. Flax and M. O'Donnell, "Phase-aberration correction using signals from point reflectors and diffuse scatterers: Basic principles," *IEEE Trans. Ultrason., Ferroelectr., Freq. Control*, vol. UFFC-35, no. 6, pp. 758–767, Nov. 1988.

[3] D. L. Liu and R. C. Waag, "Correction of ultrasonic wavefront distortion using backpropagation and a reference waveform method for time-shift compensation," *J. Acoust. Soc. Amer.*, vol. 96, no. 2, pp. 649–660, 1994.

[4] G. Chau, M. Jakovljevic, R. Lavarello, and J. Dahl, "A locally adaptive phase aberration correction (LAPAC) method for synthetic aperture sequences," *Ultrason. Imag.*, vol. 41, no. 6, pp. 3–16, 2018.

[5] R. Ali and J. J. Dahl, "Distributed phase aberration correction techniques based on local sound speed estimates," in *Proc. IEEE Int. Ultrason. Symp. (IUS)*, Oct. 2018, pp. 1–4.

[6] R. Ali, J. Jennings, and J. J. Dahl, "Medical pulse-echo ultrasound imaging based on the cross-correlation of transmitted and backpropagated-receive wavefields," in *Proc. IEEE Int. Ultrason. Symp. (IUS)*, Sep. 2020, pp. 1–4.

[7] H.-M. Schwab and G. Schmitz, "Full-wave ultrasound reconstruction with linear arrays based on a Fourier split-step approach," in *Proc. IEEE Int. Ultrason. Symp. (IUS)*, Oct. 2018, pp. 1–4.

[8] P. Stähli, M. Kuriakose, M. Frenz, and M. Jaeger, "Improved forward model for quantitative pulse-echo speed-of-sound imaging," *Ultrasonics*, vol. 108, Dec. 2020, Art. no. 106168.

[9] S. J. Sanabria, E. Ozkan, M. Rominger, and O. Goksel, "Spatial domain reconstruction for imaging speed-of-sound with pulse-echo ultrasound: Simulation and *in vivo* study," *Phys. Med. Biol.*, vol. 63, no. 21, Oct. 2018, Art. no. 215015.

[10] R. Rau, D. Schweizer, V. Vishnevskiy, and O. Goksel, "Speed-of-sound imaging using diverging waves," 2019, *arXiv:1910.05935*.

[11] M. Jaeger, G. Held, S. Peeters, S. Preisser, M. Grünig, and M. Frenz, "Computed ultrasound tomography in echo mode for imaging speed of sound using pulse-echo sonography: Proof of principle," *Ultrasound Med. Biol.*, vol. 41, no. 1, pp. 235–250, Jan. 2015.

[12] A. S. Podkowa and M. L. Oelze, "The convolutional interpretation of registration-based plane wave steered pulse-echo local sound speed estimators," *Phys. Med. Biol.*, vol. 65, no. 2, Jan. 2020, Art. no. 025003.

[13] M. Jakovljevic, S. Hsieh, R. Ali, G. C. L. Kung, D. Hyun, and J. J. Dahl, "Local speed of sound estimation in tissue using pulse-echo ultrasound: Model-based approach," *J. Acoust. Soc. Amer.*, vol. 144, no. 1, pp. 254–266, 2018.

[14] M. Dioguardi Burgio *et al.*, "Ultrasonic adaptive sound speed estimation for the diagnosis and quantification of hepatic steatosis: A pilot study," *Ultraschall der Medizin Eur. J. Ultrasound*, vol. 40, no. 6, pp. 722–733, Dec. 2019.

[15] M. Imbault *et al.*, "Ultrasonic fat fraction quantification using *in vivo* adaptive sound speed estimation," *Phys. Med. Biol.*, vol. 63, no. 21, Oct. 2018, Art. no. 215013.

[16] R. Ali and J. J. Dahl, "Travel-time tomography for local sound speed reconstruction using average sound speeds," in *Proc. IEEE Int. Ultrason. Symp. (IUS)*, Oct. 2019, pp. 2007–2010.

[17] M. Jaeger, E. Robinson, H. G. Akarcay, and M. Frenz, "Full correction for spatially distributed speed-of-sound in echo ultrasound based on measuring aberration delays via transmit beam steering," *Phys. Med. Biol.*, vol. 60, no. 11, p. 4497, 2015.

[18] J. A. Sethian and A. M. Popovici, "3-D traveltime computation using the fast marching method," *Geophysics*, vol. 64, no. 2, pp. 516–523, Mar. 1999.

[19] P. K. Kitanidis, "Parameter uncertainty in estimation of spatial functions: Bayesian analysis," *Water Resour. Res.*, vol. 22, no. 4, pp. 499–507, Apr. 1986.

[20] U. Vyas and D. Christensen, "Ultrasound beam simulations in inhomogeneous tissue geometries using the hybrid angular spectrum method," *IEEE Trans. Ultrason., Ferroelectr., Freq. Control*, vol. 59, no. 6, pp. 1093–1100, Jun. 2012.

[21] R. Ali, "Fourier-based synthetic-aperture imaging for arbitrary transmissions by cross-correlation of transmitted and received wave-fields," *Ultrason. Imag.*, vol. 43, no. 5, pp. 282—294, 2021.

[22] P. L. Stoffa, J. T. Fokkema, R. M. de Luna Freire, and W. P. Kessinger, "Split-step Fourier migration," *Geophysics*, vol. 55, no. 4, pp. 410–421, Apr. 1990.

[23] H.-M. Schwab, A. Ihrig, D. Depke, S. Hermann, M. Schafers, and G. Schmitz, "Aberration correction in photoacoustic imaging using paraxial backpropagation," in *Proc. IEEE Int. Ultrason. Symp. (IUS)*, Sep. 2017, pp. 1–4.

[24] R. Mallart and M. Fink, "Adaptive focusing in scattering media through sound-speed inhomogeneities: The van Cittert Zernike approach and focusing criterion," *J. Acoust. Soc. Amer.*, vol. 96, no. 6, pp. 3721–3732, 1994.

[25] B. E. Treeby and B. T. Cox, "K-wave: MATLAB toolbox for the simulation and reconstruction of photoacoustic wave fields," *J. Biomed. Opt.*, vol. 15, no. 2, 2010, Art. no. 021314.

[26] T. D. Mast, L. M. Hinkelman, M. J. Orr, V. W. Sparrow, and R. C. Waag, "Simulation of ultrasonic pulse propagation through the abdominal wall," *J. Acoust. Soc. Amer.*, vol. 102, no. 2, pp. 1177–1190, 1997.

[27] R. Ali, C. D. Herickhoff, D. Hyun, J. J. Dahl, and N. Bottenus, "Extending retrospective encoding for robust recovery of the multistatic data set," *IEEE Trans. Ultrason., Ferroelectr., Freq. Control*, vol. 67, no. 5, pp. 943–956, May 2020.

[28] I. Masoni, J.-L. Boelle, R. Brossier, and J. Virieux, "Layer stripping FWI for surface waves," in *Proc. SEG Tech. Program Expanded Abstr.*, Sep. 2016, pp. 1369–1373.

[29] P. Dewangan and I. Tsvankin, "Velocity-independent layer stripping of PP and PS reflection traveltimes," *Geophysics*, vol. 71, no. 4, pp. U59–U65, Jul. 2006.

[30] G. C.-H. Ng, "The application of translating transmit apertures in adaptive ultrasonic imaging," Ph.D. dissertation, Dept. Biomed. Eng., Duke Univ., Durham, NC, USA, 1997.

[31] G. C. Ng, P. D. Freiburger, W. F. Walker, and G. E. Trahey, "A speckle target adaptive imaging technique in the presence of distributed aberrations," *IEEE Trans. Ultrason., Ferroelectr., Freq. Control*, vol. 44, no. 1, pp. 140–151, Jan. 1997.

[32] C. Chen, G. A. G. M. Hendriks, R. J. G. van Sloun, H. H. G. Hansen, and C. L. de Korte, "Improved plane-wave ultrasound beamforming by incorporating angular weighting and coherent compounding in Fourier domain," *IEEE Trans. Ultrason., Ferroelectr., Freq. Control*, vol. 65, no. 5, pp. 749–765, May 2018.

[33] P. Sava and B. Biondi, "Wave-equation migration velocity analysis. I. Theory," *Geophys. Prospecting*, vol. 52, no. 6, pp. 593–606, Nov. 2004.

[34] F. Perrone, P. Sava, C. Andreoletti, and N. Bienati, "Linearized wave-equation migration velocity analysis by image warping," *Geophysics*, vol. 79, no. 2, pp. S35–S46, Mar. 2014.

[35] B. Byram, K. Dei, J. Tierney, and D. Dumont, "A model and regularization scheme for ultrasonic beamforming clutter reduction," *IEEE Trans. Ultrason., Ferroelectr., Freq. Control*, vol. 62, no. 11, pp. 1913–1927, Nov. 2015.

[36] J. Shin and L. Huang, "Spatial prediction filtering of acoustic clutter and random noise in medical ultrasound imaging," *IEEE Trans. Med. Imag.*, vol. 36, no. 2, pp. 396–406, Feb. 2017.

[37] L. L. Brickson, D. Hyun, M. Jakovljevic, and J. J. Dahl, "Reverberation noise suppression in ultrasound channel signals using a 3D fully convolutional neural network," *IEEE Trans. Med. Imag.*, vol. 40, no. 4, pp. 1184–1195, Apr. 2021.

Rehman Ali (Student Member, IEEE) received the B.S. degree in biomedical engineering from the Georgia Institute of Technology, Atlanta, GA, USA, in 2016, and the M.S. degree in computational and mathematical engineering and the Ph.D. degree in electrical engineering from Stanford University, Palo Alto, CA, USA, in 2020 and 2022, respectively.

He is currently at the laboratory of Dr. Nebojsa Duric, University of Rochester, Rochester, NY, USA, to develop waveform inversion reconstruction techniques for imaging acoustic tissue properties using ultrasound computed tomography. His research interests include signal processing, inverse problems, computational modeling of acoustics, and real-time beamforming algorithms.

Thurston Brevett (Student Member, IEEE) received the B.S. degree in electrical engineering from Northeastern University, Boston, MA, USA, in 2018, and the M.S. degree in electrical engineering (specializing in signal processing and optimization) from Stanford University, Palo Alto, CA, USA, in 2020, where he is currently pursuing the Ph.D. degree with the Department of Electrical Engineering.

His research interests include signal processing and optimization and sound speed estimation for ultrasound imaging systems.

Mr. Brevett is a fellow of the National Science Foundation (NSF), the Graduate Research Fellowships Program (GRFP), the Graduate Engineering Minority (GEM), and the Enhancing Diversity in Graduate Education (EDGE).

Dongwoon Hyun (Member, IEEE) received the B.S.E. and Ph.D. degrees in biomedical engineering from Duke University, Durham, NC, USA, in 2010 and 2017, respectively.

He is currently a Research Engineer and an Instructor with the Department of Radiology, Stanford University, Stanford, CA, USA. His current research interests include machine learning methods for beamforming, molecular ultrasound imaging, and real-time software beamforming.

Leandra L. Brickson (Student Member, IEEE) received the B.S. degree in electrical engineering from the University of Minnesota, Minneapolis, MN, USA, in 2012, and the M.S. degree in electrical engineering from North Carolina State University, Raleigh, NC, USA, in 2015. She is currently pursuing the Ph.D. degree in electrical engineering with Stanford University, Palo Alto, CA, USA.

Her background include optics, light transport, and fabrication, with research focused on image processing and deep learning of ultrasound images and volumes under the supervision of Dr. Jeremy Dahl. Her research interests include biomedical applications of machine learning using deep learning and reinforcement learning.

Jeremy J. Dahl (Senior Member, IEEE) received the B.S. degree in electrical engineering from the University of Cincinnati, Cincinnati, OH, USA, in 1999, and the Ph.D. degree in biomedical engineering from Duke University, Durham, NC, USA, in 2004.

He is currently an Associate Professor with the Department of Radiology, Stanford University, Stanford, CA, USA. His current research interests include beamforming, coherence and noise in ultrasonic imaging, speed of sound estimation, and ultrasound radiation force imaging technology.